



HAL
open science

Tuning nanomechanical properties of microstructures made by 3D direct laser writing

Mehdi Belqat, Xingyu Wu, Laura Piedad Chia Gomez, Jean-Pierre Malval,
Sébastien Dominici, Benjamin Leuschel, Arnaud Spangenberg, Karine Mougin

► **To cite this version:**

Mehdi Belqat, Xingyu Wu, Laura Piedad Chia Gomez, Jean-Pierre Malval, Sébastien Dominici, et al.. Tuning nanomechanical properties of microstructures made by 3D direct laser writing. Additive Manufacturing, 2021, 47, pp.102232. 10.1016/j.addma.2021.102232 . hal-03426111

HAL Id: hal-03426111

<https://hal.science/hal-03426111>

Submitted on 15 Nov 2021

HAL is a multi-disciplinary open access archive for the deposit and dissemination of scientific research documents, whether they are published or not. The documents may come from teaching and research institutions in France or abroad, or from public or private research centers.

L'archive ouverte pluridisciplinaire **HAL**, est destinée au dépôt et à la diffusion de documents scientifiques de niveau recherche, publiés ou non, émanant des établissements d'enseignement et de recherche français ou étrangers, des laboratoires publics ou privés.

1 **Tuning nanomechanical properties of**
2 **microstructures made by 3D direct laser writing**

3 *Mehdi Belqat^{1,2}, Xingyu Wu^{1,2}, Laura Piedad Chia Gomez^{1,2}, Jean-Pierre Malval^{1,2}, Sébastien*
4 *Dominici^{1,2}, Benjamin Leuschel^{1,2} Arnaud Spangenberg^{1,2}, Karine Mougin^{1,2}*

5
6 ¹Université de Haute-Alsace, CNRS, IS2M UMR 7361, F-68100 Mulhouse, France

7 ²Université de Strasbourg, France

8 Corresponding Authors: karine.mougin@uha.fr, arnaud.spangenberg@uha.fr

9 **KEYWORDS:** Two photon polymerization, Micro-additive manufacturing, Atomic Force Microscopy,
10 Young's modulus, 3D direct laser writing

24
25
26
27
28
29
30
31
32
33
34
35
36
37
38
39
40
41
42
43
44
45
46
47
48
49
50
51
52

ABSTRACT

3D Direct laser writing (3D DLW) based on two photon polymerization represents a powerful technique for the additive manufacturing of 3D micro- and nano-structures, which have a number of promising applications in areas including biology and cell cultures up to soft robotic. New applications often entail the contact and movement of nanoscale areas, therefore understanding of the mechanical properties involved in such systems is necessary for creating reliable micro and nanoscale applications. Notably, knowledge about nanomechanics of 3D printed structures and its dependence on its geometry and contact size remains essential. This study focuses on the investigation of the Young's modulus of 3D printed microstructures by Atomic Force Microscopy. Using the PeakForce QNM AFM mode, it was possible to determine the influence of the laser power and the monomer and their mixture on the micromechanical properties, in particular the Young's modulus. The fabricated structures are 2D structures, consisting of successive lines forming a square. Three different resins have been used based on poly(ethyleneglycol)diacrylate (PEGDA), trimethylolpropane triacrylate (TMPTA) and pentaerythritol triacrylate (PETA). The results obtained show that the increase in laser power increases the Young's modulus of these raw materials, since it induces a stronger crosslinking density. Mixtures of resins have also been formulated inducing a Young's modulus structure increase when increasing the amount of PETA. By combining these two approaches, tuning of the nanomechanical properties of the final microstructures on an unprecedented range covering 3 orders of magnitude, from MPa up to GPa have been successfully achieved. This major result paves the way to in-depth reflection on future works in nanorobotics or biomedical devices, where complex mechanical behavior are highly desired.

53 1. Introduction

54 Characterization of mechanical properties of structures and materials are of primary importance for their
55 use in a broad range of applications. The first known scientific research on the mechanics of building
56 elements dates back only to the end of the 16th century with the famous work of Galileo on the tension
57 and bending of beams. But, science has evolved and last century has brought new characterization
58 techniques that have been developed to face it. In parallel, new generation of materials and complex
59 composites have also been created and built at different scales. Among the various fabrication
60 techniques available to shape the material, 3D direct laser writing (3D DLW) based on two photon
61 polymerization represents a powerful technique for the fabrication of 3D micro- and nano-structures [1-
62 3]. This technique allows to perfectly replicate miniaturized 3D objects, process that could not be
63 achieved with traditional microfabrication technologies such as self-assembly technique [4], electron
64 beam lithography [5] and nanoimprint lithography [6]. In addition, physico-chemical and mechanical
65 properties of these microstructures can be easily tuned by varying different technical parameters such as
66 nature of resins, laser power and writing speed [7-9]. However, the characterization of such micro-
67 objects remains difficult, while the control of the mechanical properties of these microstructures is
68 essential for their future applications. Indeed, the measurement of the Young's modulus of micro-
69 objects is crucial to achieve the microstructures with a high fidelity. For instance, in bioengineering,
70 tuning rigidity of a scaffold or a prosthesis allows to enhance the biocompatibility of the objects in its
71 new environment [10]. In addition, the detection of a mechanical defect on a microstructure can avoid a
72 real damage in its bulk or on its surface.

73 Nevertheless, measuring mechanical properties of micro-objects via conventional methods is impossible
74 due to the size of these objects. In order to circumvent these limitations, several characterization
75 techniques have been proposed and developed to study the mechanical properties of micro and
76 nanostructures. Treacy *et al.* [11] have estimated the Young's modulus of isolated carbon nanotubes by
77 measuring, in transmission electron microscopy, the amplitude of their intrinsic thermal vibration. This
78 original method, although highly powerful, can only be used for specific and conductive micromaterials

79 such as carbon nanotubes. The three-point bending test is commonly used to test the bending strength of
80 materials. Inspired from this principle, Lemma *et al.* [12] have proposed a bending characterization
81 method of the mechanical properties of microstructures produced by two-photon stereolithography.
82 They have combined static and dynamic mechanical analysis on pillar-like structures and picometer-
83 sensitive laser Doppler vibrometry of drum-like structures to viably and nondestructively estimate
84 Young's modulus, Poisson's ratio, and density of 3D printed micromaterials. This innovative and non-
85 destructive method can however only be used for microstructures having a specific shape. Shin *et al.*
86 [13] have proposed another method to induce microbending in microstructures and to determine their
87 Young's modulus. For this, microcantilever bars were manufactured and at the end of these structures, a
88 microsphere was fabricated in order to induce bending using optical tweezers. The sphere was then
89 trapped by an optical beam and was able to move over several microns depending on the strength of the
90 optical trap. Young's modulus of the microcantilever could be indirectly estimated from the deviation of
91 the bar during the optical stress. Other destructive techniques such as *in situ* mechanical test in scanning
92 electronic microscope could have been used to estimate mechanical properties. Geer *et al.* [14] have
93 measured deformation of fractal-like architectures by micro-compression test and developed a
94 computational model that was able to capture local stress distributions within the nanolattices under this
95 solicitation. As a result, they could explain some of the underlying deformation mechanisms and
96 validate the measured effective stiffness of the metamaterial such as for 3D microprinted Eiffel Tower.
97 Finally, micro and nanoindentation remains one of the most commonly used tools independently of its
98 destructive character. The principal goal of a nanoindentation test is to extract elastic modulus and
99 hardness of a specimen material from experimental readings of the indenter load versus the depth of
100 penetration. Lee *et al.* [15] have used the microindentation technique to determine the Young's modulus
101 and compressive strength of different architectures (square, pillars and metamaterials) at the
102 micrometric scale. In a different way, Oakdale *et al.* [16] sought to assess the influence of density as
103 well as the influence of UV post-polymerization on Young's modulus by conducting compression tests
104 on Woodpiles using a nanoindenter. Young's moduli were extracted from the slope of the load curves.
105 Bauer *et al.* [17] did similar compressive and destructive tests at microscale on pyrolyzed resins to

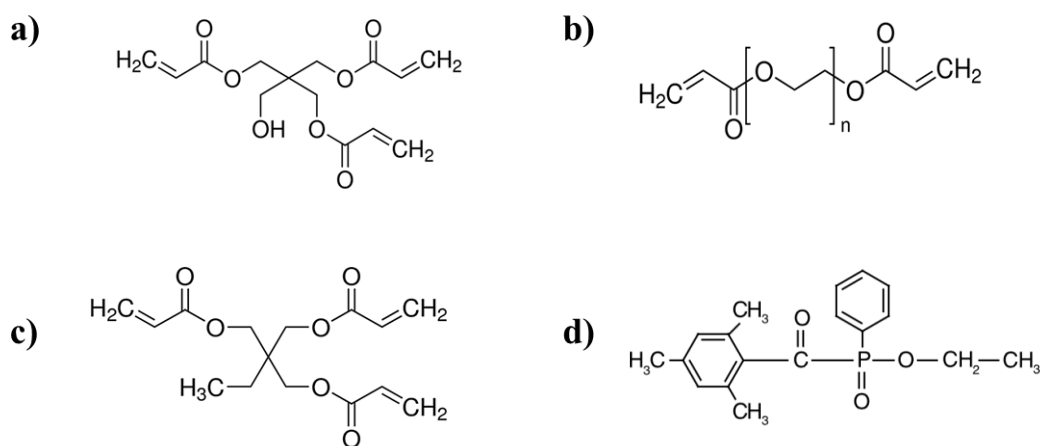
106 determine the influence of the size of carbon nanolattices as well as the influence of an alumina coating
107 on the Young's modulus of the 3D-printed microstructures. Lastly, Barner-Kowollik *et al.* [18] have
108 used nanodynamical mechanical analysis (NanoDMA) to investigate the bulk viscoelastic properties
109 (hardness, complex elastic modulus, and loss factor) of the microstructures over the course of irradiation
110 of polymer at the nanoscale. This technique is a quite new and powerful technology to characterize the
111 bulky mechanical properties of microstructures produced by 3D DLW. In a complementary approach,
112 Atomic Force Microscopy in PeakForce QNM mode, which also represents an impressive and non-
113 destructive test, allows determining mechanical properties of microstructure surface. Gou *et al.* [19]
114 have investigated the mechanical properties of hydrogels produced by two-photon stereolithography
115 using atomic force microscopy. In the Quantitative Nanomechanical Property Mapping (QNM) mode,
116 they were able to determine the influence of the manufacturing laser power on the Young's modulus on
117 their different 3D printed samples. All these different examples have shown that new generation of
118 technics have been developed to allow determining the intrinsic mechanical properties of 3D printed
119 microstructures depending on their geometry, nature and size. Thus, the knowledge of fundamental
120 nanomechanics mechanism of these micromaterials remains essential. Even though the stakes are so
121 high regarding the targeting applications, the influence of the fabrication parameters on mechanical
122 properties are not systematically investigated when designing new advanced materials.

123 In this study, we have proposed to investigate three different photosensitive resins, PEGDA
124 (Poly(ethyleneglycol)diacrylate), Trimethylolpropane Triacrylate (TMPTA) and PETA (Pentaerythritol
125 triacrylate) to create microstructures of varying stiffness by 3D DLW. The apparent Young moduli of
126 these materials have been determined by AFM in PeakForce QNM. Two parameters such as the
127 increase of the laser power and the type of resins mixture have allowed to tune the nanomechanical
128 properties of the final microstructures on a large range, from MPa up to GPa. These results pave the
129 way to in-depth reflection on future works in nanorobotics or cell biology, where complex mechanical
130 behavior are highly desired.

131 **2. Materials and Methods**

132 **2.1. Materials**

133 Pentaerythritol triacrylate (PETA) ($\rho = 1,18 \text{ g/ml}$; $M = 298,29 \text{ g/mol}$) and Poly(ethylene Glycol)
 134 diacrylate PEGDA ($\rho = 1,12 \text{ g/ml}$; $M = 700 \text{ g/mol}$) were purchased from Sigma-Aldrich. Diphenyl
 135 (2,4,6- trimethylbenzoyl)- phosphine oxide (TPO-L) was purchased from BASF ($M = 336,371 \text{ g/mol}$).
 136 Trimethylolpropane Triacrylate (TMPTA) was kindly provided by Sartomer ($\rho = 1,1 \text{ g/ml}$; $M = 296,32$
 137 g/mol). The chemical formula of all the products are depicted in Figure 1.



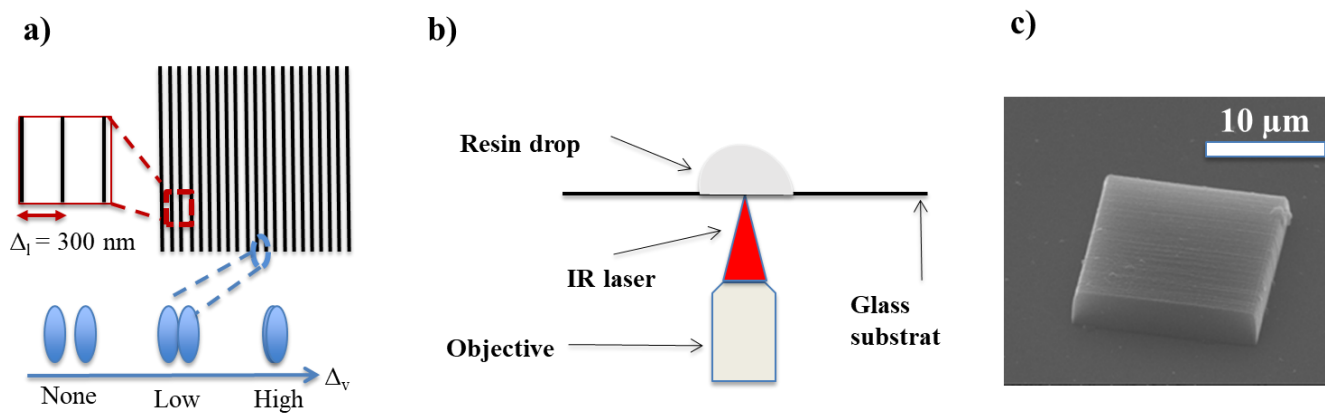
138

139 **Figure 1.** Chemical formula : a) PETA; b) PEGDA ; c) TMPTA ; d) TPO-L.

140 2.2. Characterization

141 2.2.1. Microfabrication by 3D DLW

142 A detailed description of the 3D microfabrication set-up has been previously described elsewhere. [8,
 143 20] However for the sake of clarity, it has to be mentioned that the generation of microstructures has
 144 been done via the computer-aided design (CAD) module of Simpoly allowing the control of specific
 145 parameters such as the percentage of overlap Δ_v between each voxel or the distance Δ_l between two lines
 146 forming the microstructure (Figure 2a). The two photon excitation was performed at 800 nm by
 147 focusing the femtosecond laser beam with an objective lens (x40, NA: 0.65) into a drop of resist (Figure
 148 2b). This substrate was previously functionalized with 3-(triethoxysilyl) propyl methacrylate to enhance
 149 the adhesion of the structures onto the substrate. The 3D microstructure is finally obtained by washing
 150 away the unreacted monomer using ethanol (Figure 2c).



151

152 **Figure 2.** 3D DLW fabrication steps of a microstructure. a) CAD modelization and writing strategy for
 153 square microstructure, b) Photofabrication based on two photon polymerization, c) SEM image of
 154 typical microstructure obtained after microprinting.

155

156 2.2.2. Atomic Force Microscopy

157 The investigation of the morphology, adhesives and mechanical properties of all the 3D microstructures
 158 have been performed by Atomic Force Microscope (AFM). A Bruker Multimode 8 AFM in Peakforce
 159 Quantitative Nanomechanics (PeakForce QNM) mode has been used to study the physico-chemical and
 160 mechanical nanoscale features of the 3D microstructures. Particularly, PeakForce QNM mode is a recent
 161 advanced mode developed by Bruker to investigate quantitative nanomechanical mapping properties
 162 with the simultaneous measurement of the sample's adhesion between tip and sample surface, Young's
 163 modulus (according to either Derjaguin-Muler-Toporov (DMT) or Sneddon model), deformation and
 164 energy dissipation along with the surface topography [21]. The imaging scan size was (5 μm x 5 μm).
 165 The physico-chemical parameters average such as roughness (RMS), adhesion and spell out this
 166 abbreviation (DMT) Module were determined using the Gwydion software. QNM etched silicon probes
 167 were provided by Bruker. They were RTESPA-150 presenting a nominal spring constant $k \sim 6$ N/m and
 168 RTESPA-300 presenting a nominal spring constant $k \sim 40$ N/m. All used tips were calibrated according
 169 to Bruker's user guide [21] and norm ISO13095:2014. The test operation steps of relative method in
 170 PeakForce QNM were described as followed: firstly, a Sapphire-15M (supplied by Bruker) was used for
 171 calibration of deflection sensitivity of cantilever. Then, the stiffness k of the cantilever was calibrated
 172 according to thermal noise method. Secondly, the k and R values were adjusted to make the acquired

173 modulus consistent with the standard values obtained with calibration samples (supplied by Bruker).
174 Thirdly, the sample was carried out. The results were analysed by both Nanoscope analysis 2.0 software
175 provide by Bruker and Gwyddion. The root mean square (RMS) roughness, adhesion and DMT
176 modulus parameters were measured for at least three representative AFM images from different areas of
177 3D microstructures, and at least three different samples for each film were studied and analysed as
178 previously described in S.Oras *et al.* [22]. The Derjaguin-Muler-Toporov (DMT) model can be viewed
179 as a modified Hertzian model, which takes into account the adhesive forces between the tip and the
180 surface. According to this approach, the reduced Young's modulus, E_r , is given by [23].

$$181 \quad E_r = \frac{3(F_{tip} - F_{adh})}{4\sqrt{Rd^3}} \quad (1)$$

182 In Eq. (1), F_{tip} is the force on the AFM tip, F_{adh} is the adhesive force between the AFM tip and sample,
183 R is the AFM tip radius, and d is the deformation depth. The reduced Young's modulus is related to the
184 sample Young's modulus (E_s) and is calculated by Eq. (2) [15].

$$185 \quad \frac{1}{E_r} = \frac{(1-\nu_s^2)}{E_s} + \frac{(1-\nu_I^2)}{E_I} \quad (2)$$

186 where E_I is the indenter Young's modulus, ν_I is the Poisson's ratio of the indenter and ν_s is Poisson's
187 ratio of the sample.

188 **2.2.3. Fourier-Transform Infrared (FTIR) microspectroscopy**

189 The investigation of the degree of conversion (DC) has been performed by FTIR microspectroscopy
190 using a Thermo Scientific Nicolet iN10 MX equipped with a germanium tip for the ATR mode.
191 Typically, the analyzed zone was 5 micrometers at the center of squared polymeric structures of 20
192 micrometers length. The absorbance spectra were measured from 4000 cm^{-1} to 675 cm^{-1} wavenumber
193 with a resolution of 8 cm^{-1} and 64 scans per spectrum. This method relies on measuring the degree of
194 conversion (DC) of the structured polymers in comparison with the resin mixture and is determined by
195 Equation (3) [24]:

196

197

$$DC = \left[1 - \frac{A_{C=C}/A_{C=O}}{A'_{C=C}/A'_{C=O}} \right] \times 100 \quad (4)$$

198

where $A_{C=C}$, $A_{C=O}$, $A'_{C=C}$ and $A'_{C=O}$ are the integrated area of absorption bands related to the C=C and

199

C=O moieties in the polymerized and the nonpolymerized resin, respectively.

200

Results and discussion

201

The size and the structure of the samples have been first optimized before investigating the influence of

202

the different parameters such as the laser power and nature of the resin on the nanomechanical

203

properties of the 3D microstructures. Indeed, it was first necessary to determine the overlap between two

204

consecutive voxels and two adjacent lines on the surface in order to minimize the roughness of the

205

sample, which might also induce an impact on the modulus and adhesion measurements. Besides, the

206

3D architecture itself and the way photopolymerization is carried out may impact the mechanical

207

responses of the microstructure [25], therefore we have limited our study to squared microstructures

208

made of a single layer. The 3D DLW manufacturing of a sample starts by focusing a beam under a

209

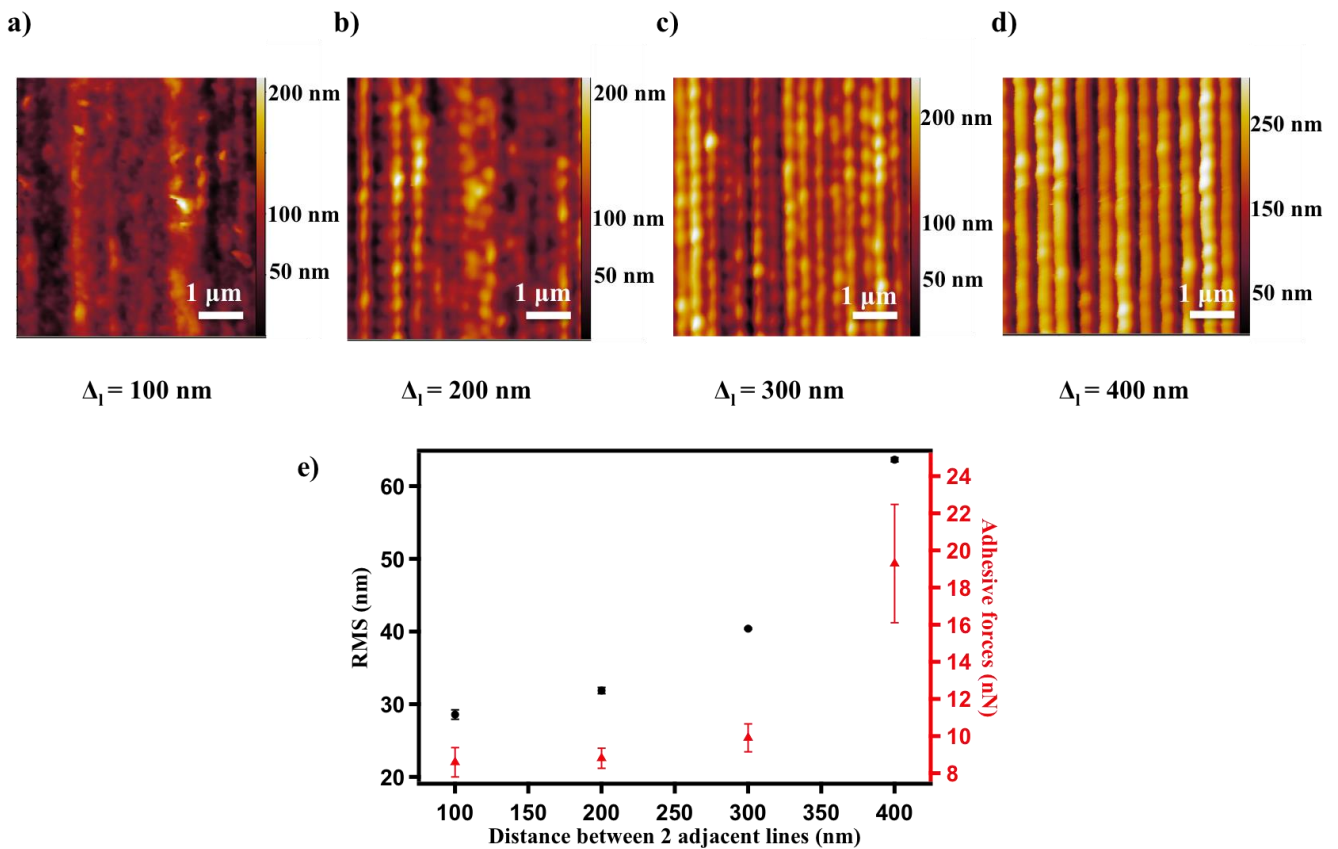
microscope resulting on the point-by-point photopolymerization of a resin. This point, corresponding to

210

a voxel, takes the form of an ellipsoid and represents the building block of the fabricated structure. The

211

overlap (Δ_v) characterizes the distance between the voxels, illustrated in Figure 2a.



212

213 **Figure 3.** a-d) AFM topography images of PETA 25x25 μm² square samples (PeakForce QNM mode)
 214 varying as function of overlap parameter. e) Graph depicting the evolution of roughness (RMS)-(black
 215 point) and adhesive forces (red triangle) as function of layer distance (Δ_l).

216

217 For a given line, this overlap parameter between two successive voxels was set at 60% in the CAD
 218 software, allowing a low roughness in the writing direction of the sample as depicted in Figure 3d.

219

The overlap (Δ_l) characterizes the distance between two adjacent lines (Figure 2a). As expected, the

220

lower the overlap is, the higher the roughness is (Figure 3). However, in case of high overlap (i.e. low

221

distance between two adjacent lines), the difference between the threshold energy and the damage

222

energy, defining the possible manufacturing window, is greatly reduced. For sake of clarity, the

223

threshold energy represents the minimum energy required by the system to initiate a

224

photopolymerization phenomenon, and the damage energy corresponds to the energy leading to the

225

sample degradation. Besides, reducing the overlap (Δ_l) can significantly increase the manufacturing

226

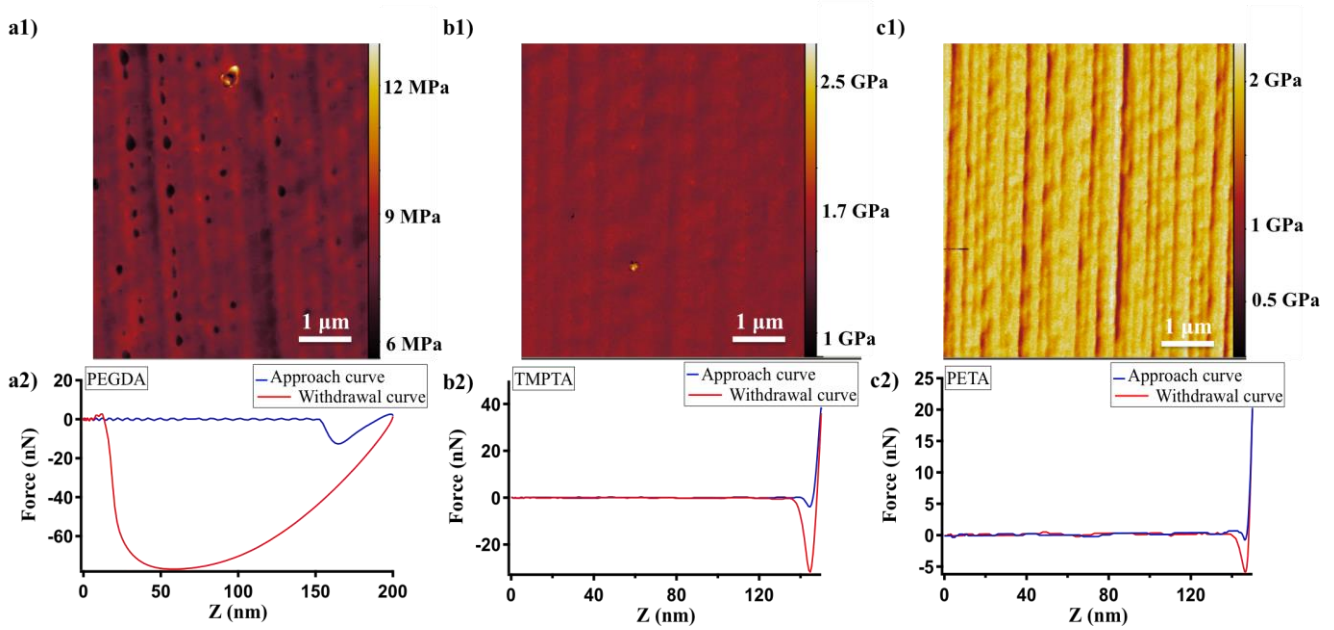
time. For instance, 25x25 μm² square microstructures used for mechanical investigations are fabricated

227

in 12 min or 3 min respectively for Δ_l = 100 nm or for Δ_l = 400 nm. In order to optimize the fabrication

228 parameters, different overlap values between two adjacent lines, have been tested and the roughness of
229 the average roughness type (Root Mean Square-RMS) and the forces of adhesion were measured by
230 AFM as observed in Figure 3. The graph in Figure 3e shows that roughness increases with the distance
231 value between two adjacent lines, as theoretically expected. Adhesion force also slowly increases with
232 this parameter, however the overall variation of the value remains weak. The latter can be explained by
233 the fact that, when the overlap is low, lines are separated and acts as single units instead of being stick
234 and/or polymerized with the adjacent ones. As a result, it increases roughness of the overall surface, and
235 it also leads to heterogeneity in chemical properties as illustrated by the evolution of error bars for
236 adhesive forces. Finally, for $\Delta_1 = 300$ nm, the roughness has been also characterized in function of the
237 average laser power and the nature of the resists used (Figures S1 to S5, and Tables S3 to S6). While for
238 a given monomer, no trends of the RMS have been noticed in function of the laser power, one can
239 observed a slightly higher RMS values for TMPTA (50 nm) and PETA (41 nm) compare to PEGDA (27
240 nm). Additionally, SEM images provided in supporting information confirm the low impact of
241 aforementioned parameters on the surface morphology of the 2D microstructures (Figures S6, S7 and
242 S8). Consequently, a distance of 300 nm between lines has been fixed in the mechanical studies
243 described hereafter.

244 Then, three different resins (PEGDA, TMPTA, PETA) have been photopolymerized using previous
245 conditions to assess the evolution of the square sample topography as well as their mechanical
246 properties (variation of their Young's modulus). Their corresponding approach-retract curves have been
247 also presented in Figure 4.



248

249 **Figure 4.** AFM topographic images in PeakForce QNM mode and their corresponding approach-retract
 250 curves: a1-2) PEGDA; b1-2) TMPTA; c1-2) PETA.

251

252 The approach-retract curves in Figure 4 a2, b2, c2 are formed by the superposition of a blue curve which
 253 corresponds to the approach curve and of a red curve corresponding to the withdrawal curve of the tip
 254 from the surface. The difference between these two curves corresponds to the energy dissipated by the
 255 tip during contact. This Hysteresis is higher for a soft material (Figure 4-a2), and smaller for a rigid
 256 material as observed in Figure 4-c2. The Young's modulus corresponding to the three different resins
 257 with distinctive processable parameters are summarized in Table 1.

258

259

260

261

262

263 **Table 1.** Young's Modulus obtained for the three different monomers PEDA, TMPTA and PETA
 264 photopolymerized (manufactured with an x40 objective N.A. 0,65) for a laser power of 9.9 mW, an
 265 exposure time of 10 ms and an overlap $\Delta_l = 300$ nm, characterized by AFM in PF QNM mode.

266

267

268

269

270

271

Monomers	DMT Young's Modulus (MPa)	Cantilever's spring constant (N/m)	Tip radius (nm)
PEGDA	6,9 +/- 0,1	6	80
TMPTA	1669 +/- 56	40	100
PETA	1956 +/- 13	40	100

272

273

274

275

276

277

278

279

280

281

282

283

284

285

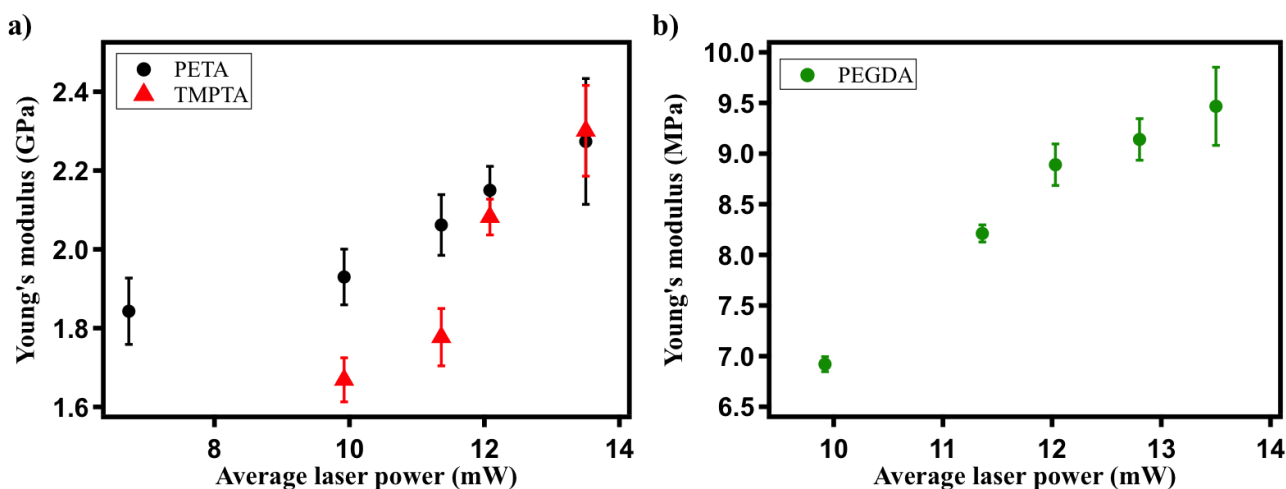
286

These results are in good agreement with literature, in particular for PEGDA [19] and PETA [12]. TMPTA and PETA have similar Young's modulus value, this can be explained by the fact that TMPTA has a similar chemical structure to PETA, as a result both resins moduli are expected to be of the same order of magnitude. In 3D DLW process, two-photon polymerization (2PP) occurs in a very limited time and space scales compare to conventional photopolymerization. Thus, additionally to oxygen inhibition, dark polymerization or functionality of monomers, many other complex phenomenon such as optical aberration or local heating have to be taken into consideration in the formation of the polymer network [26]. However, as described by E. Andrzejewska [27], the process of network formation for free radical photopolymerization is strongly linked to the kinetics of photopolymerization. The functionality, defined here as the number of polymerizable groups per molecule, play a crucial role both on the kinetics and on the formation of higher cross-link density. Indeed, higher functionality involves higher concentration of functional groups which in turn leads to a faster formation of denser network. Therefore, one can expect higher cross-link density, and consequently higher Young's modulus in PETA and TMPTA compare to PEGDA as observed in Figure 4. Once the system was calibrated, it was possible to assess the influence of the laser power as well as that of the monomer mixture on the resin Young's modulus.

287

3.1 Influence of the laser power

288 The PETA, TMPTA and PEGDA samples were generated under the same conditions with an overlap Δ_l
289 = 300nm. The results obtained are presented in Figure 5.
290



291
292 **Figure 5.** Evolution of Young's modulus as function of laser power for a) PETA (black circles) and
293 TMPTA (red triangles), b) PEGDA (green circles).

294
295 From a general point of view, an increase in Young's modulus is observed as a function of writing laser
296 power independantly of the nature of the monomer. For PETA, Young's modulus varies from 1.85 GPa
297 for a power of 6.73 mW up to 2.27 GPa for a power of 13.5 mW (Figure 5a). Such behavior is expected
298 since the size of an individual voxel and the corresponding mechanical properties of the material are
299 directly related to the energy of the laser pulse and the duration of exposure. Lu *et al.* [24] demonstrated
300 a direct link between the laser power and the degree of conversion and therefore, by extension, the
301 crosslinking density. Previous analyzes have shown that crosslink density is directly related to modulus
302 of elasticity and ultimate tensile strength of crosslinked acrylic materials [28]. By comparison, Lemma
303 *et al.* [12] observed an increase in Young's modulus of 1.5 GPa for a power of 8.5 mW at 2 GPa at 16
304 mW, measured by micro-bending on an IP-L 780 resin (mainly composed of PETA monomer). The
305 order of magnitude remains the same, however the values obtained by the latter are lower, which can be
306 explained by different experimental conditions (numerical aperture of the microscope objective, overlap
307 between each voxel, nature and concentration of photoinitiator, etc...).

308 For TMPTA, the results obtained are presented in Figure 5a. A similar behavior as PETA has been
309 observed, with an increase in Young's modulus as a function of laser power. Indeed, Young's modulus
310 varies from 1.67 GPa for a laser power of 9.9 mW to 2.3 GPa for a power of 13.5 mW. However, in
311 comparison with PETA, it seems that the increase is more significant (increase of 38 % compared to 23
312 % for PETA). Chemically, both monomers have the same number of acrylic functions however, PETA
313 is more viscous (500-1000 cP) than TMPTA (80-135 cP) due to the possibility of forming hydrogen
314 bonds via the hydroxy group (-OH). While it is known that initial viscosity of acrylate based resist can
315 drastically enhanced the reactivity of a given resists [29], further investigation will be necessary to state
316 on the role of viscosity on mechanical properties. More broadly, the viscosity has been scarcely
317 investigated in the frame of a two-photon polymerization as recently reported by Zandrini and
318 coworkers [30].

319 Finally, the evolution of mechanical properties of the PEGDA is displayed in Figure 5b. An increase in
320 the Young's modulus is observed as a function of the laser power, the Young's modulus varied from 6.9
321 MPa for a power of 9.9 mW to 9.5 MPa for a power of 13.5 mW, constituting an increase of 38 %. The
322 lower modulus values can be explained by the presence of only two acrylate functions for PEGDA
323 instead of three for PETA or TMPTA. Thus, a looser crosslinking network can be generally observed for
324 mono- or difunctional monomers. Finally, unlike other studies where PEGDA is used as a hydrogel, it
325 should be noted that in our formulation, no solvent has been used, which explains values of the order of
326 MPa. In addition, in presence of water, photopolymerized materials can exhibit Young's moduli of the
327 order of a few hundred kPa.

328 To conclude, the results obtained confirm the link between the final Young's modulus of the material
329 and the manufacturing laser power, but also the influence of viscosity and the chemical nature of
330 monomer on the mechanical properties of the material.

331

332

333

334

3.2 Influence of the monomer Mixture

In order to be able to modulate the mechanical properties of the microstructures over a wider range, several mixtures of PETA and PEGDA have been prepared to assess the chemical influence on their Young's modulus. The results obtained are summarized in the graph in Figure 6a.

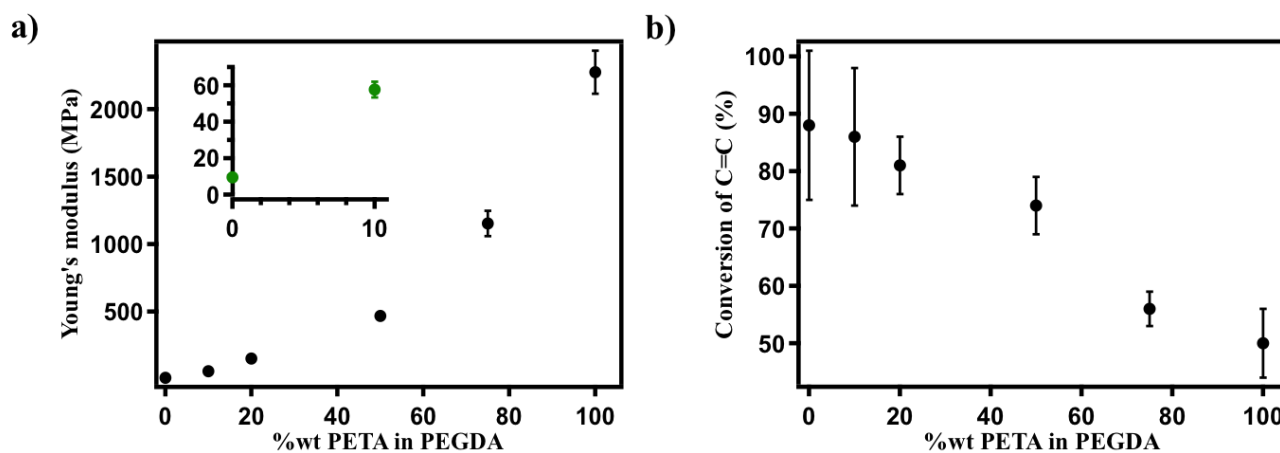


Figure 6. Evolution of a) Young's modulus and of b) degree of conversion as function of PETA concentration in PEGDA for a laser power of 13.5 mW, an exposure time of 10 ms and an overlap $\Delta_l = 300\text{nm}$. The Young's moduli obtained for 0 and 10 % of PETA in PEGDA have been highlighted in inset (Green markers).

An increase in Young's modulus is observed as a function of the PETA concentration. Indeed, the addition of 10% wt PETA induces an increase of the modulus from 9.4 MPa up to 57 MPa. At 20% PETA, the modulus reaches 150 MPa. For equal mixture, the Young's modulus increases to nearly 500 MPa and to 1.15 GPa, when the amount of PETA is equal to 75%. On the other hand, Figure 6b depicts the evolution of the degree of conversion (DC) with the increase in PETA concentration in the final mixture. The DC of polymerized microstructures have been determined using ATR-FTIR microspectroscopy as proposed early by Cicha and coworkers [31]. Representative FTIR spectra for different mixtures before and after polymerization are given in the supporting information (Figure S11). Briefly, a value of 55% of conversion is determined in case of 100% of PETA. This result is in good agreement with the work of Jiang *et al.* where a degree of conversion of 42% is determined by using Raman microspectroscopy for a commercial resin, namely IP-L 780 which is mainly composed of

356 PETA [24]. Besides, a value higher than 80% of conversion is observed for a microstructure made of
357 100% of PEGDA. Due to lack of sensitivity in our experimental set-up, we can not say with certainty
358 the absolute value, however the fact that this value is higher than the one reported for PETA is
359 consistent with the fact that monomer of higher functionality leads to lower conversion [27]. Finally,
360 contrary to what it has been noticed for mixture of monomers by Jiang *et al.* [32], when the
361 concentration of PETA increase from 0 to 100 wt% in the mixture, the degree of conversion is
362 progressively decreasing as expected. The latter highlights the impact of the monomer structure and
363 concentration on the final degree of conversion.

364 These overall results show that by tuning the mixture of two monomers, it has been possible to modulate
365 by 3 orders of magnitude (10 MPa, 100 MPa and 1000 MPa), the mechanical properties of 3D
366 microstructures produced by 3D DLW, opening up new perspectives for the fabrication of devices with
367 complex behavior. In addition to those varied technical parameters, the writing speed remains also
368 another key parameter that strongly impacts the Young's modulus of 3D microstructures, and which has
369 also to be taken under consideration when designing new microdevices.

370

371 **3. Conclusion**

372 This research work deals with the need to finely control the mechanical properties of 3D micro-objects
373 produced by 3D DLW. Hence, evolution of the young's modulus of photopolymerized square
374 microstructures has been investigated by AFM in PeakForce QNM mode, which represents an essential
375 technique for the physico-chemical analysis of the surfaces of micrometric objects. Three main
376 monomers commonly used in 3D DLW have been tested. Results have shown that it was possible to
377 measure the apparent Young's moduli ranging from MPa to GPa at microscale. This parameter has
378 allowed to first assess the impact of photonic manufacturing parameters on the final mechanical
379 properties of the material at microscale. Particularly, it appears that the increase in laser power induces
380 an increase in mechanical properties. Second, the influence of the monomer on the mechanical
381 properties has also been highlighted. It follows that the nature and structure of the monomer have a
382 direct influence on the Young's modulus. Third, it was possible to modulate over a wide range (3 orders

383 of magnitude) the mechanical properties by acting on a mixture of monomers. This latter approach
384 opens up new perspectives in fields where complex deformations of the manufactured object are desired
385 (nanorobotics, nanosurgery) or where 3D spatial encoding of chemical and mechanical clues are highly
386 desired (cell biology, organ on chip, tissue engineering). Up to now, the variation of mechanical
387 properties remains moderate with regard to the challenges in terms of complexity required to develop
388 adaptive structures or multi-functional structures for the above mentioned applications such as
389 nanorobotics or cell biology. Thus, new routes should be kept in being explored.

390

391

392

393 ACKNOWLEDGMENT

394 The authors thanks the Agence Nationale de la recherche (Project ANR 2PhotonInsight: ANR-16-CE08-
395 0020) and Institut Carnot MICA for financial support. This work was also partially supported by an
396 Institutional Research Grant (MIPPI4D) from the Région Grand Est.

397

398 REFERENCES

399

400 [1] S. Maruo, O. Nakamura, S. Kawata, Three-dimensional microfabrication with two-photon-absorbed
401 photopolymerization. *Opt. Lett.* **1997**, 2 (22), 132–134.

402 [2] C. N LaFratta, J. T Fourkas, T. Baldacchini,; R. A. Farrer, Multiphoton Fabrication. *Angew. Chem.,*
403 *Int. Ed.* **2007**, 46, 6238–6258.

404 [3] C. Barner-Kowollik, M. Bastmeyer, E. Blasco, G. Delaittre, P. Müller, B. Richter, M. Wegener, 3D
405 Laser Micro- and Nanoprinting: Challenges for Chemistry. *Angew. Chem., Int. Ed.* **2017**, 56 (50), 15828-
406 15845.

407 [4] G.M. Whitesides, J.P. Mathias, C.T. Seto. Molecular Self-Assembly and Nanochemistry: A Chemical
408 Strategy for the Synthesis of Nanostructures. *Science (80-.).* **1991**, 254, 1312–1319.

409 [5] I. Haller, M. Hatzakis, R. Srinivasan. High-resolution Positive Resists for Electron-beam Exposure.
410 *IBM J. Res. Dev.* **1968**, 12 (3), 251–256.

- 411 [6] S.-W. Lee, K.-S. Lee, J. Ahn, et al. Highly Sensitive Biosensing Using Arrays of Plasmonic Au
412 Nanodisks Realized by Nanoimprint Lithography. *ACS Nano* **2011**, 5 (2), 897–904.
- 413 [7] M. Hippler, E. Blasco, J. Qu, M. Tanaka, C. Barner-Kowollik, M. Wegener, M. Bastmeyer.
414 Controlling the shape of 3D microstructures by temperature and light. *Nature Communications* **2019**, 10,
415 232.
- 416 [8] L.P. Chia Gomez, A. Spangenberg, X.-A. Ton, Y. Fuchs, F. Bokeloh, J.-P. Malval, B. Tse Sum Bui,
417 D. Thuau, C. Ayela, K. Haupt, O. Soppera, Rapid prototyping of chemical microsensors based on
418 molecularly imprinted polymers synthesized by two-photon stereolithography. *Adv. Mater.* **2016**, 28 (28),
419 5931-5937.
- 420 [9] S.-Y. Yu, G. Schrodj, K. Mougin, J. Dentzer, J.-P. Malval, H.-W. Zan, O. Soppera, A. Spangenberg,
421 A. Direct Laser Writing of Crystallized TiO₂ and TiO₂ /Carbon Microstructures with Tunable Conductive
422 Properties. *Adv. Mater.* **2018**, 30, 1805093.
- 423 [10] R. O’Rorke, T. Steele, H. Taylor. Bioinspired fibrillar adhesives: A review of analytical models and
424 experimental evidence for adhesion enhancement by surface patterns. *J. Adhes. Sci. Technol.* **2015**, 30.
- 425 [11] M.M.J. Treacy, T.W. Ebbesen, J.M. Gibson. Exceptionally high Young’s modulus observed for
426 individual carbon nanotubes. *Nature*. **1996**, 381 (6584), 678–680.
- 427 [12] E.D. Lemma, F. Rizzi, T. Dattoma, et al. Mechanical Properties Tunability of Three-Dimensional
428 Polymeric Structures in Two-Photon Lithography. *IEEE Trans. Nanotechnol.* **2017**, 16 (1), 23–31.
- 429 [13] C.-S. Shin, T.-J. Li, C.-L. Lin. Alleviating Distortion and Improving the Young’s Modulus in Two-
430 Photon Polymerization Fabrications. *Micromachines*. **2018**, 9 (12), 615.
- 431 [14] L.R. Meza, A.J. Zelhofer, N. Clarke, et al. Resilient 3D hierarchical architected metamaterials. *Proc.*
432 *Natl. Acad. Sci.* **2015**, 112 (37), 11502–11507.
- 433 [15] J.H. Lee, J.P. Singer, E.L. Thomas. Micro-/nanostructured mechanical metamaterials. *Adv. Mater.*
434 **2012**, 24 (36), 4782–4810.
- 435 [16] J.S. Oakdale, J. Ye, W.L. Smith, J. Biener. Post-print UV curing method for improving the
436 mechanical properties of prototypes derived from two-photon lithography. *Opt. Express*. **2016**, 24 (24),
437 27077.

- 438 [17] J. Bauer, A. Schroer, R. Schwaiger, O. Kraft. Approaching theoretical strength in glassy carbon
439 nanolattices. *Nat. Mater.* **2016**, 15 (4), 438–443.
- 440 [18] M. Gernhardt, E. Blasco, M. Hippler, et al. Tailoring the Mechanical Properties of 3D
441 Microstructures Using Visible Light Post-Manufacturing. *Adv. Mater.* **2019**, 31 (30), 1901269.
- 442 [19] X. Gou, M. Zheng, Y. Zhao, et al. Mechanical property of PEG hydrogel and the 3D red blood cell
443 microstructures fabricated by two-photon polymerization. *Appl. Surf. Sci.* **2017**, 416, 273–280.
- 444 [20] M. Jin, J. Xie, a J-P. Malval, A. Spangenberg, O. Soppera, D-L. Versace, T. Leclerc, H. Pan, D. Wan,
445 H. Pu, P. Baldeck, O. Poizat, S. Knopf. Two-photon lithography in visible and NIR ranges using
446 multibranch-based sensitizers for efficient acid generation. *J. Mater. Chem. C* **2014**, 2, 7201.
- 447 [21] Bruker PeakForce tapping brochure [https://www.bruker.com/content/bruker/int/en/products-and-](https://www.bruker.com/content/bruker/int/en/products-and-solutions/microscopes/materials-afm/afm-modes/peakforce-tapping.html)
448 [solutions/microscopes/materials-afm/afm-modes/peakforce-tapping.html](https://www.bruker.com/content/bruker/int/en/products-and-solutions/microscopes/materials-afm/afm-modes/peakforce-tapping.html)
- 449 [22] S.Oras, S.Vlassov, M. Berholts, R. Lohmus, K. Mougín, Tuning adhesion forces between
450 functionalized gold colloidal nanoparticles and silicon AFM tips: role of Ligands and capillary forces
451 *Beilstein J. Nanotechnol.* **2018**, 9, 660–670.
- 452 [23] B.. Derjaguin, V.. Muller, Y.. Toporov. Effect of contact deformations on the adhesion of particles.
453 *J. Colloid Interface Sci.* **1975**, 53 (2), 314–326.
- 454 [24] L.J. Jiang, Y.S. Zhou, W. Xiong, et al. Two-photon polymerization: investigation of chemical and
455 mechanical properties of resins using Raman microspectroscopy. *Opt. Lett.* **2014**, 39 (10), 3034–3037.
- 456 [25] S. Juodkazis, V. Mizeikis, K. Khuen Seet, H. Misawaa, U. G. K. Wegst, Mechanical properties and
457 tuning of three-dimensional polymeric photonic crystals. *Appl. Phys. Lett.* **2007**, 91, 241904.
- 458 [26] E. Skliutas, M. Lebedevaite, E. Kabouraki, T. Baldacchini, J. Ostrauskaite, M. Vamvakaki, M.
459 Farsari, S. Juodkazis, M. Malinauskas. Polymerization mechanisms initiated by spatio-temporally
460 confined light. *Nanophotonics* **2021**; 10(4): 1211–1242
- 461 [27] E. Andrzejewska. Photopolymerization kinetics of multifunctional monomers. *Progress in Polymer*
462 *Science*, **2001**, 26, 605-665.

- 463 [28] T. Baldacchini, M. Zimmerley, C.-H. Kuo, E.O. Potma, R. Zadoyan. Characterization of
464 microstructures fabricated by two-photon polymerization using coherent anti-stokes Raman scattering
465 microscopy. *J. Phys. Chem. B* **2009**, 113 (38), 12663–12668.
- 466 [29] A. Marcinkowska, E. Andrzejewska. Viscosity Effects in the Photopolymerization of Two-
467 Monomer Systems. *Journal of Applied Polymer Science*, **2010**, 116, 280–287.
- 468 [30] T. Zandrini, N. Liaros, L.J. Jiang, Y.F. Lu, J.T. Fourkas, R. Osellame, T. Baldacchini. Effect of the
469 resin viscosity on the writing properties of two-photon polymerization. *Optical Materials Express*, **2019**,
470 9 (6), 2601-2616.
- 471 [31] K. Cicha, Z. Li, K. Stadlmann, A. Ovsianikov, R. Markut-Kohl, R. Liska, J. Stampfl. Evaluation of
472 3D structures fabricated with two-photon-photopolymerization by using FTIR spectroscopy. *Journal of*
473 *Applied Physics*, **2011**, 110, 064911
- 474 [32] L. Jiang, W. Xiong, Y. Zhou, Y. Liu, X. Huang, D. Li, T. Baldacchini, L. Jiang, Y. Lu.
475 Performance comparison of acrylic and thiolacrylic resins in two-photon polymerization. *Optics*
476 *Express*, **2016**, 24 (12), 13687-13701.

477

478

479

480

481

482

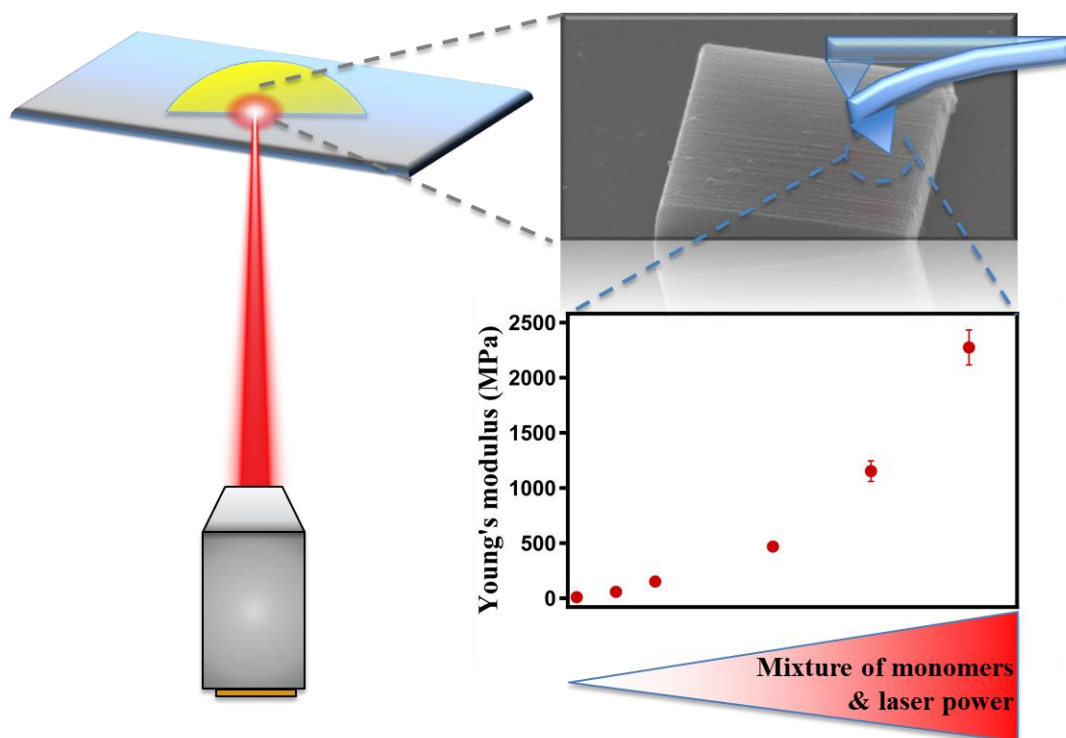
483

484

485

486
487
488
489
490
491
492
493
494
495
496
497
498
499
500
501

For Graphical Abstract Only



502
503
504
505
506
507
508
509
510
511
512

513 **Tuning nanomechanical properties of**
514 **microstructures made by 3D direct laser writing**

515 *Mehdi Belqat^{1,2}, Xingyu Wu^{1,2}, Laura Piedad Chia Gomez^{1,2}, Jean-Pierre Malval^{1,2}, Sébastien*
516 *Dominici^{1,2}, Benjamin Leuschel^{1,2}, Arnaud Spangenberg^{1,2}, Karine Mougin^{1,2}*

517
518 ¹Université de Haute-Alsace, CNRS, IS2M UMR 7361, F-68100 Mulhouse, France

519 ²Université de Strasbourg, France

520 Corresponding Authors: karine.mougin@uha.fr, arnaud.spangenberg@uha.fr

521
522
523
524 **Supporting Information**

525
526
527
528
529
530
531
532
533
534
535
536

537 **Table of contents**

538 **1. Definition or calculation of studied parameters**

539 **Table S1** : Studied parameters and their typical used values

540 **Table S2** : Average laser powers and the respective peak irradiance

541 **2. Roughness analysis**

542 **Table S3** : RMS roughness and Young's modulus of PETA in function of average laser power.

543 **Figure S1** : Topography image (left) and Young's modulus image (right) of PETA fabricated at an
544 average laser power of $P = 6.73$ mW. RMS = 36.36 nm and $E = 1.84$ GPa.

545 **Table S4** : RMS roughness and Young's modulus of TMPTA in function of average laser power.

546 **Figure S2** : Topography image (left) and Young's modulus image (right) of TMPTA fabricated at an
547 average laser power of $P = 9.93$ mW. RMS = 51.65 nm and $E = 1.67$ GPa.

548 **Table S5** : RMS roughness and Young's modulus of PEGDA in function of average laser power.

549 **Figure S3** : Topography image (left) and Young's modulus image (right) of PEGDA fabricated at an
550 average laser power of $P = 9.93$ mW. RMS = 27.1 nm and $E = 6.92$ MPa.

551 **Table S6**: RMS roughness and Young's modulus of different mixtures of PETA and PEGDA

552 **Figure S4**: Topography image (left) and Young's modulus image (right) of 10%PETA-90%PEGDA
553 fabricated at an average laser power of $P = 13.5$ mW. RMS = 26.48 nm and $E = 57.6$ MPa.

554 **Figure S5** : Topography image (left) and Young's modulus image (right) of 20%PETA-80%PEGDA
555 fabricated at an average laser power of $P = 13.5$ mW. RMS = 36.89 nm and $E = 151.4$ MPa.

556 **Figure S6** : Topography image (left) and Young's modulus image (right) of 50%PETA-50%PEGDA
557 fabricated at an average laser power of $P = 13.5$ mW. RMS = 36.94 nm and $E = 468$ MPa.

558 **Figure S7**: Topography image (left) and Young's modulus image (right) of 75%PETA-25%PEGDA
559 fabricated at an average laser power of $P = 13.5$ mW. RMS = 45.34 nm and $E = 1153$ MPa

560 **3. Morphology characterizations**

561 **Figure S8** : SEM images of 2D PETA structures made by 3D DLW at A) 6.73 mW, B) 11.36 mW, C)
562 13.5 mW

563 **Figure S9** : SEM images of 2D PEGDA structures made by 3D DLW at A) 9.92 mW, B) 10.92, C) 13.5
564 mW.

565 **Figure S10** : SEM images of 2D structures made by 3D DLW from mixture of PETA and PEGDA: A)
566 10%PETA-90%PEGDA, B) 20%PETA-80%PEGDA, C) 50%PETA-50%PEGDA, D) 75%PETA-
567 25%PEGDA.

568 **4. Determination of degree of conversion by FTIR microspectroscopy**

569 **Figure S11** : FTIR spectra of resins with different weight percentages of PETA and PEGDA (blue
570 lines) and the corresponding two-photon polymerized squares (red lines, laser power 13.5 mW was used
571 for all squares).

572

573 **1. Definition or calculation of studied parameters**

574 **Table S1** : Studied parameters and their typical used values

Parameter	Value
Wavelength λ ¹	800 nm
Repetition rate f ¹	80 MHz
Pulse duration τ ¹	140 fs
Numerical aperture NA ¹	0.65
Lateral dimension d_l ¹	1.5 μm
Exposure time t_{exp} ¹	10 ms
Slicing Δ ¹	300 nm
Pulse Energy E	84.1 pJ – 168.8 pJ
Average laser power P_a	6.73 – 13.5 mW
Peak irradiance I ²	0.009 – 0.019 TW/cm ²

575 ¹N.B.: all these parameters are kept constant for the current study. Only the average laser power is tuned.

576 ²N.B.: the peak irradiance I is sometimes referred to as “intensity”.

577 Lateral dimension, pulse energy and peak irradiance are calculated according to equations (1), (2) and (3)
 578 respectively. Lateral dimension of the voxel is calculated thanks to the equation:

579
$$d_l = \frac{1.22 \times \lambda}{NA} \quad (1)$$

580 where λ is the excitation wavelength, NA the numerical aperture of the objective. Pulse energy E is then
 581 calculated using equation (2) :

582
$$E = \frac{P_a}{f} \quad (2)$$

583 where P_a is the average power in W and f the repetition rate in Hz. Peak irradiance is finally obtained
 584 thanks to the following equation :

585
$$I = \frac{2E}{\pi \cdot d_l^2 \cdot \tau \cdot \sqrt{\pi}} \quad (3)$$

586 where τ is the pulse duration.

587 **Table S2** : Average laser powers and the respective peak irradiance

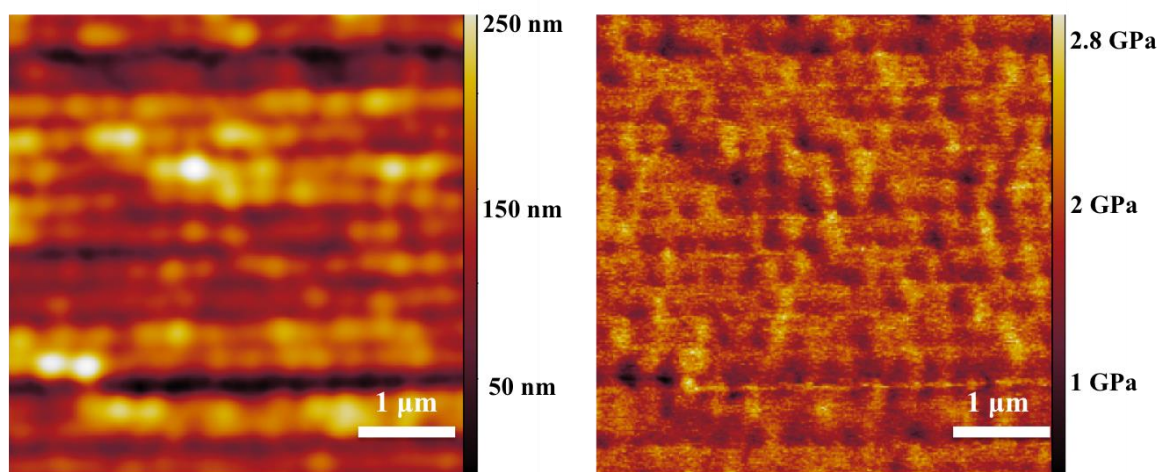
Average laser power (mW)	Peak irradiance (TW/cm ²)
6.73	9.59 x 10 ⁻³
9.92	14.1 x 10 ⁻³
11.36	16.1 x 10 ⁻³
12.03	17.1 x 10 ⁻³
12.8	18.2 x 10 ⁻³
13.5	19.2 x 10 ⁻³

588 **2. Roughness analysis:** The root mean square (RMS) roughness was used to measure the surface
 589 roughness of the several samples fabricated during this study. The RMS roughness and Young's modulus
 590 obtained for each monomers at different average laser powers are presented in Tables S3, S4 and S5
 591 corresponding to PETA, TMPTA and PEGDA respectively. Besides, topography and Young's modulus
 592 images obtained by AFM are presented for the 3 monomers at the energy threshold (Figure S1 to S3), as
 593 well as for two mixtures (20 and 50% PETA, Figure S4 and S5).

594
 595
 596 **Table S3 :** RMS roughness and Young's modulus of PETA in function of average laser power.

Average laser power (mW)	RMS roughness (nm)	Young's Modulus (GPa)	Stdev (GPa)
6.73	39.36	1.843	0.08
9.92	44.31	1.93	0.07
11.36	34.94	2.062	0.08
12.08	39.26	2.15	0.06
13.5	48.61	2.274	0.16

597
 598
 599
 600



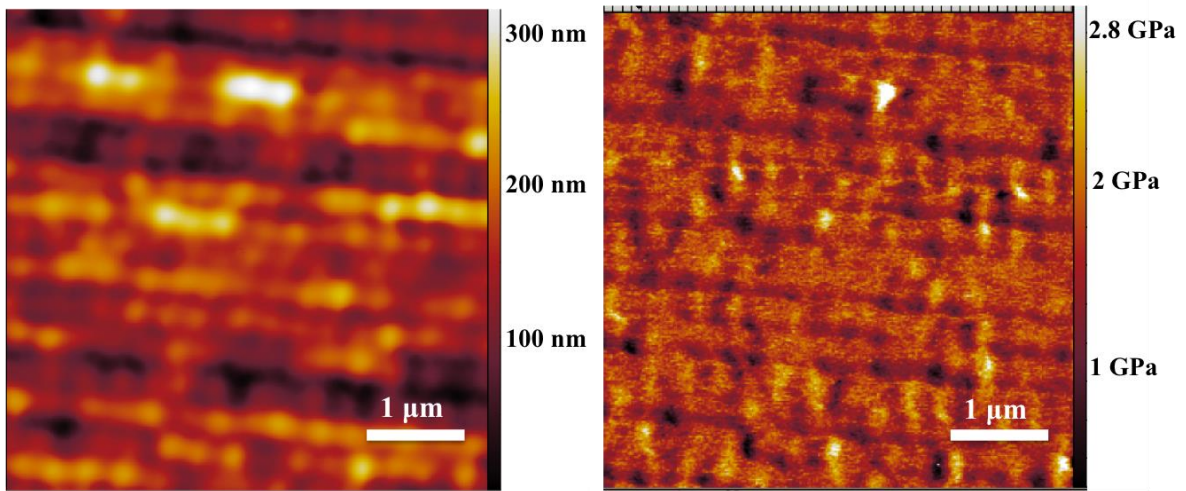
601
 602 **Figure S1 :** Topography image (left) and Young's modulus image (right) of PETA fabricated at an
 603 average laser power of $P = 6.73$ mW. $RMS = 36.36$ nm and $E = 1.84$ GPa.

604
 605
 606
 607

608 **Table S4** : RMS roughness and Young's modulus of TMPTA in function of average laser power.

Average laser power (mW)	RMS roughness (nm)	Young's Modulus (GPa)	Stdev (GPa)
9.92	51.65	1.67	0.06
11.36	50.83	1.77	0.07
12.08	50.9	2.08	0.05
13.5	47.7	2.3	0.11

609



610

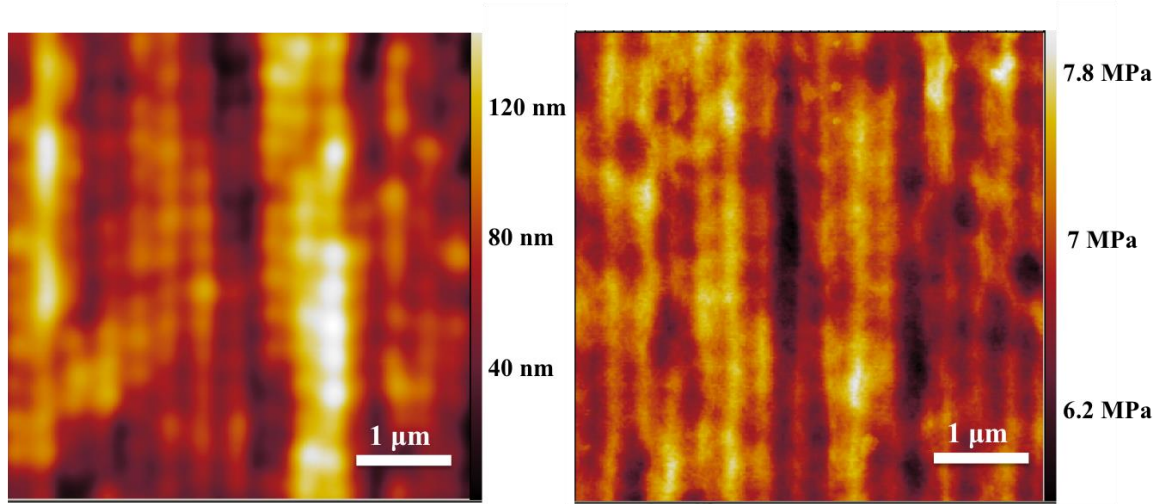
611 **Figure S2** : Topography image (left) and Young's modulus image (right) of TMPTA fabricated at an
 612 average laser power of $P = 9.93$ mW. RMS = 51.65 nm and $E = 1.67$ GPa.

613

614 **Table S5** : RMS roughness and Young's modulus of PEGDA in function of average laser power.

Average laser power (mW)	RMS roughness (nm)	Young's Modulus (MPa)	Stdev (MPa)
9.92	27.1	6.92	0.07
11.36	20	8.21	0.08
12.03	30.9	8.89	0.2
12.8	28	9.14	0.2
13.5	26.9	9.47	0.38

615



616

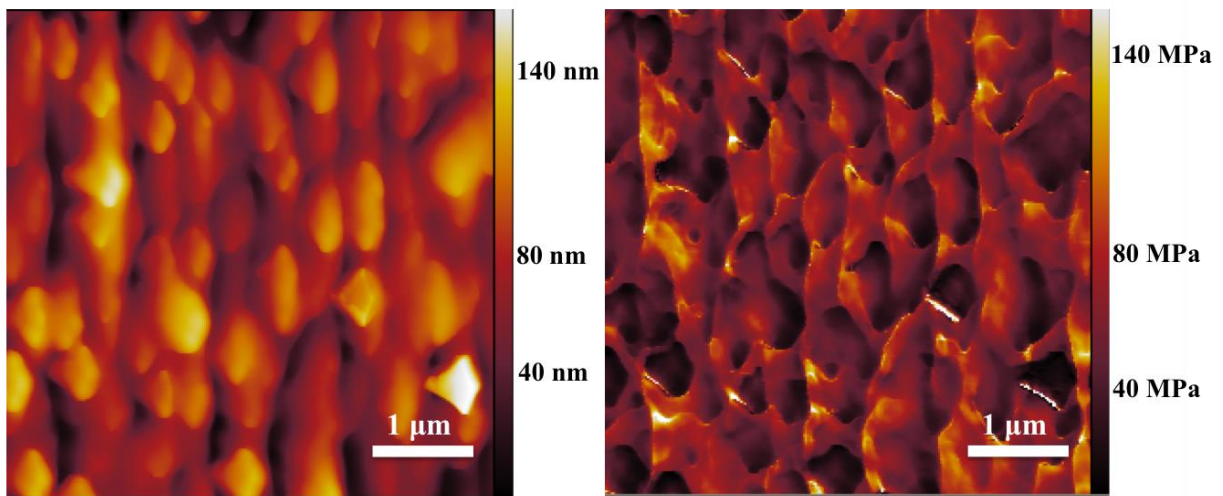
617 **Figure S3 :** Topography image (left) and Young's modulus image (right) of PEGDA fabricated at an
 618 average laser power of $P = 9.93$ mW. $RMS = 27.1$ nm and $E = 6.92$ MPa.

619

620 **Table S6:** RMS roughness and Young's modulus of different mixtures of PETA and PEGDA.

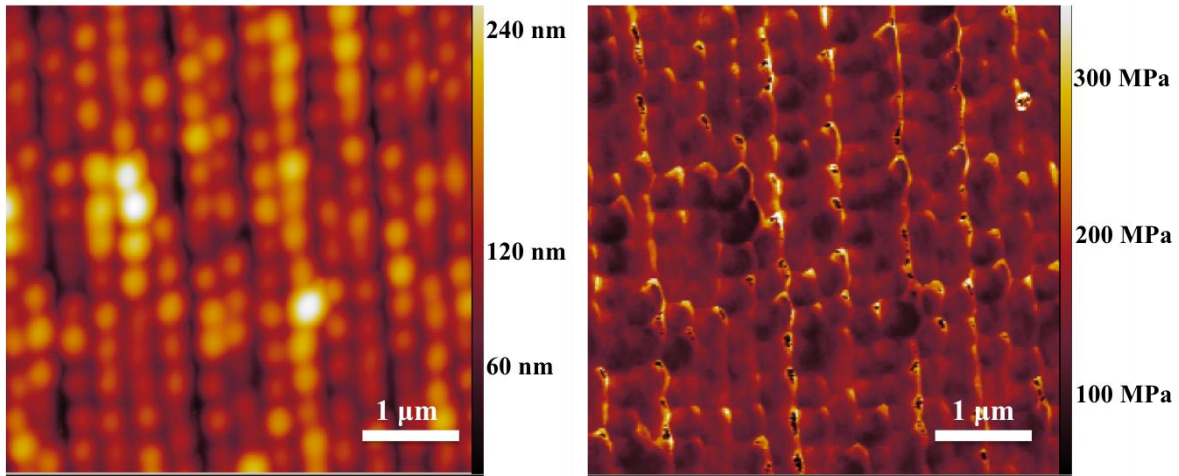
Mixture	RMS roughness (nm)	Young's Modulus (MPa)	Stdev (MPa)
10%PETA – 90% PEGDA	26.48	57.6	4.3
20%PETA – 80% PEGDA	36.89	151.4	9
50%PETA – 50% PEGDA	36.94	468	16.7
75%PETA – 25% PEGDA	45.34	1153	93.9

621



622

623 **Figure S4:** Topography image (left) and Young's modulus image (right) of 10%PETA-90%PEGDA
 624 fabricated at an average laser power of $P = 13.5$ mW. $RMS = 26.48$ nm and $E = 57.6$ MPa.

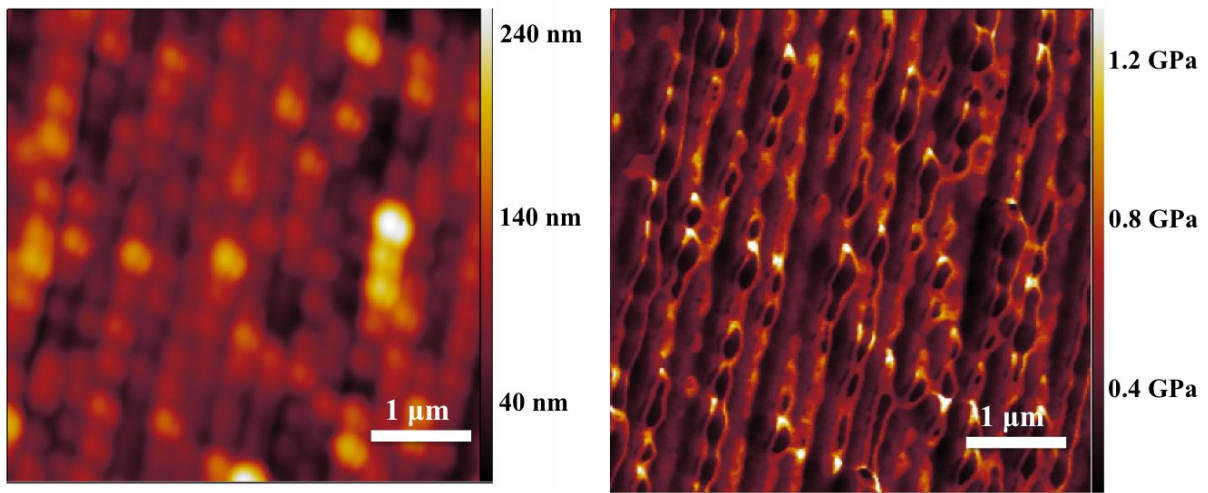


625

626

627

Figure S5 : Topography image (left) and Young's modulus image (right) of 20%PETA-80%PEGDA fabricated at an average laser power of $P = 13.5$ mW. RMS = 36.89 nm and $E = 151.4$ MPa.

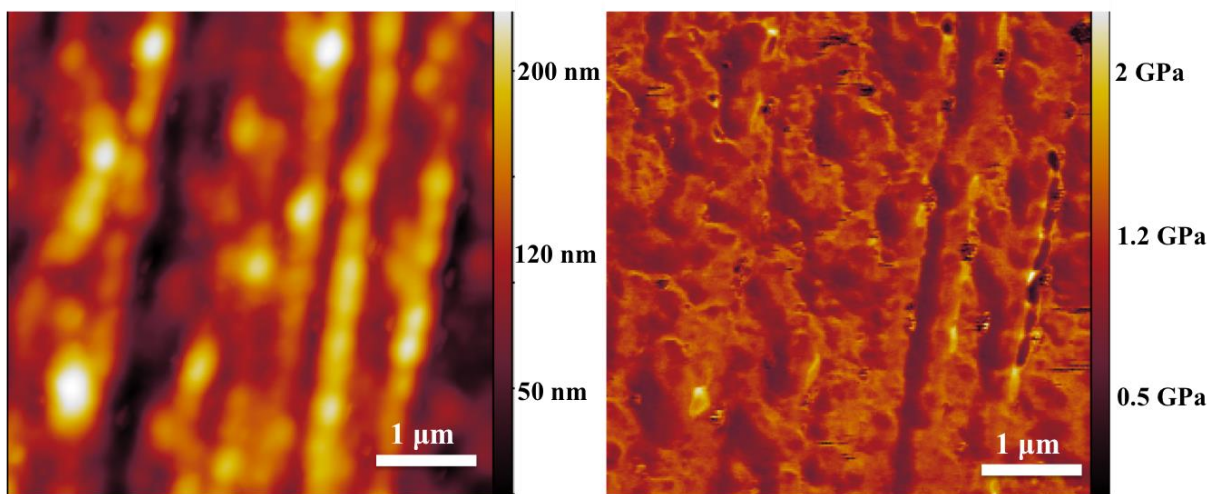


628

629

630

Figure S6 : Topography image (left) and Young's modulus image (right) of 50%PETA-50%PEGDA fabricated at an average laser power of $P = 13.5$ mW. RMS = 36.94 nm and $E = 468$ MPa.



631

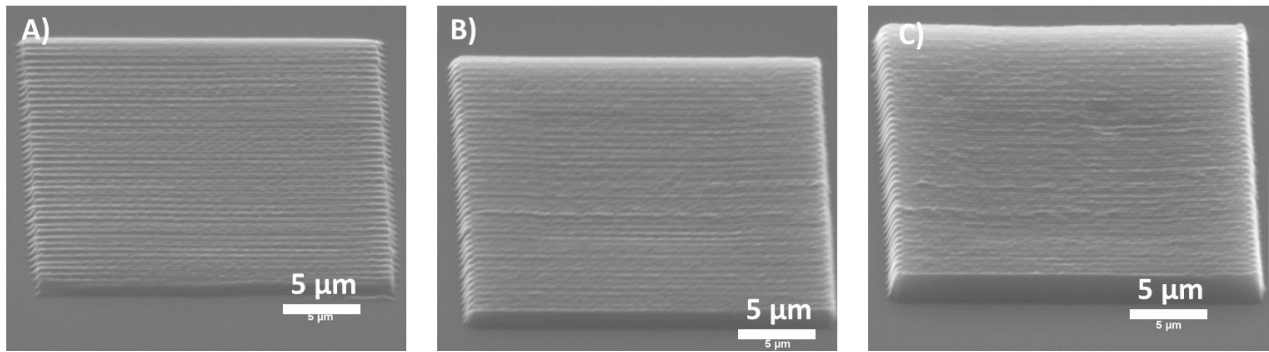
632

633

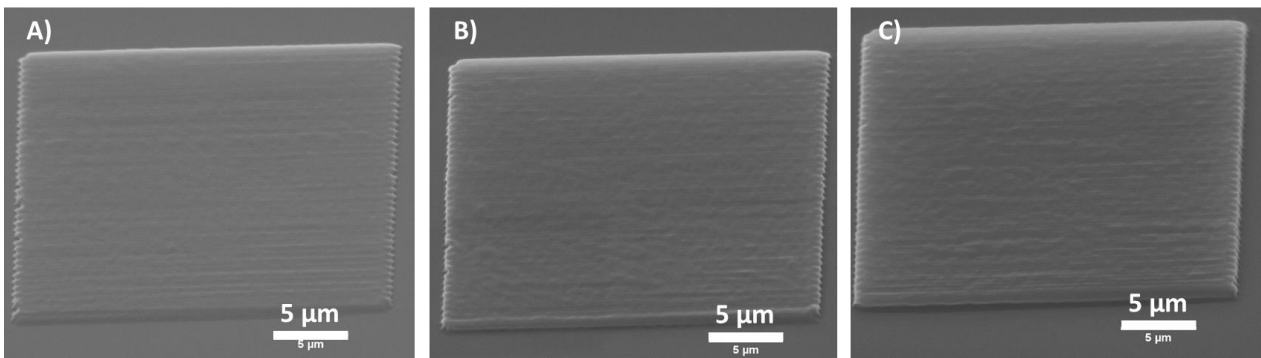
Figure S7: Topography image (left) and Young's modulus image (right) of 75%PETA-25%PEGDA fabricated at an average laser power of $P = 13.5$ mW. RMS = 45.34 nm and $E = 1039$ MPa.

634

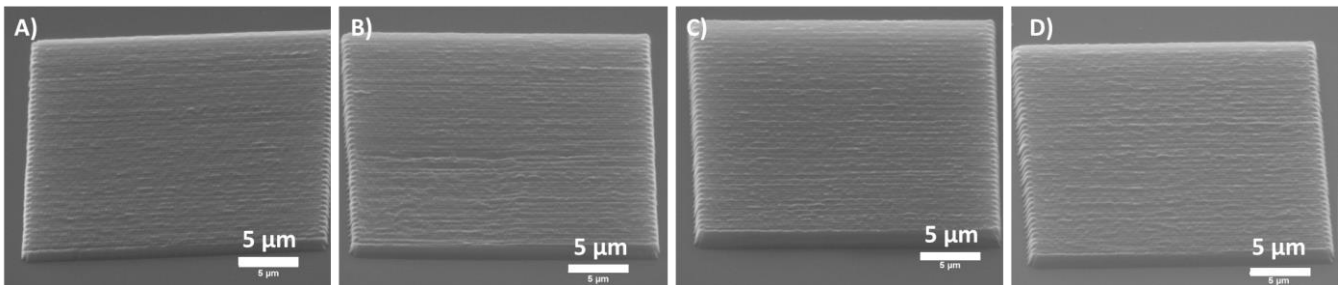
635 **3. Morphology characterization by scanning electron microscopy (SEM):**



636 **Figure S8 :** SEM images of 2D PETA structures made by 3D DLW at A) 6.73 mW, B) 11.36 mW, C)
637 13.5 mW.



638 **Figure S9 :** SEM images of 2D PEGDA structures made by 3D DLW at A) 9.92 mW, B) 10.92, C) 13.5
639 mW.



641 **Figure S10 :** SEM images of 2D structures made by 3D DLW from mixture of PETA and PEGDA: A)
642 10%PETA-90%PEGDA, B) 20%PETA-80%PEGDA, C) 50%PETA-50%PEGDA, D) 75%PETA-
643 25%PEGDA.

644 **4. Determination of the degree of conversion (DC) by ATR FTIR microspectroscopy :**

645 Micro-FTIR (Fourier-Transform Infrared spectroscopy) tests were performed with a Thermo Scientific
646 Nicolet iN10 MX on polymers squares of 20 micrometers length using a germanium tip ATR. The
647 analyzed zone was 5 micrometers at the center of the squares. The absorbance spectra were measured
648 from 4000 cm^{-1} to 675 cm^{-1} wavenumber with a resolution of 8 cm^{-1} and 64 scans per spectrum. This
649 method relies on measuring the degree of conversion (DC) of the structured polymers in comparison
650 with the resin mixture. The determination of the DC allow to quantify the amount of consumed carbon-
651

652 carbon double bonds (C=C) during the photopolymerization. It is determined using the following
653 equation from [1]:

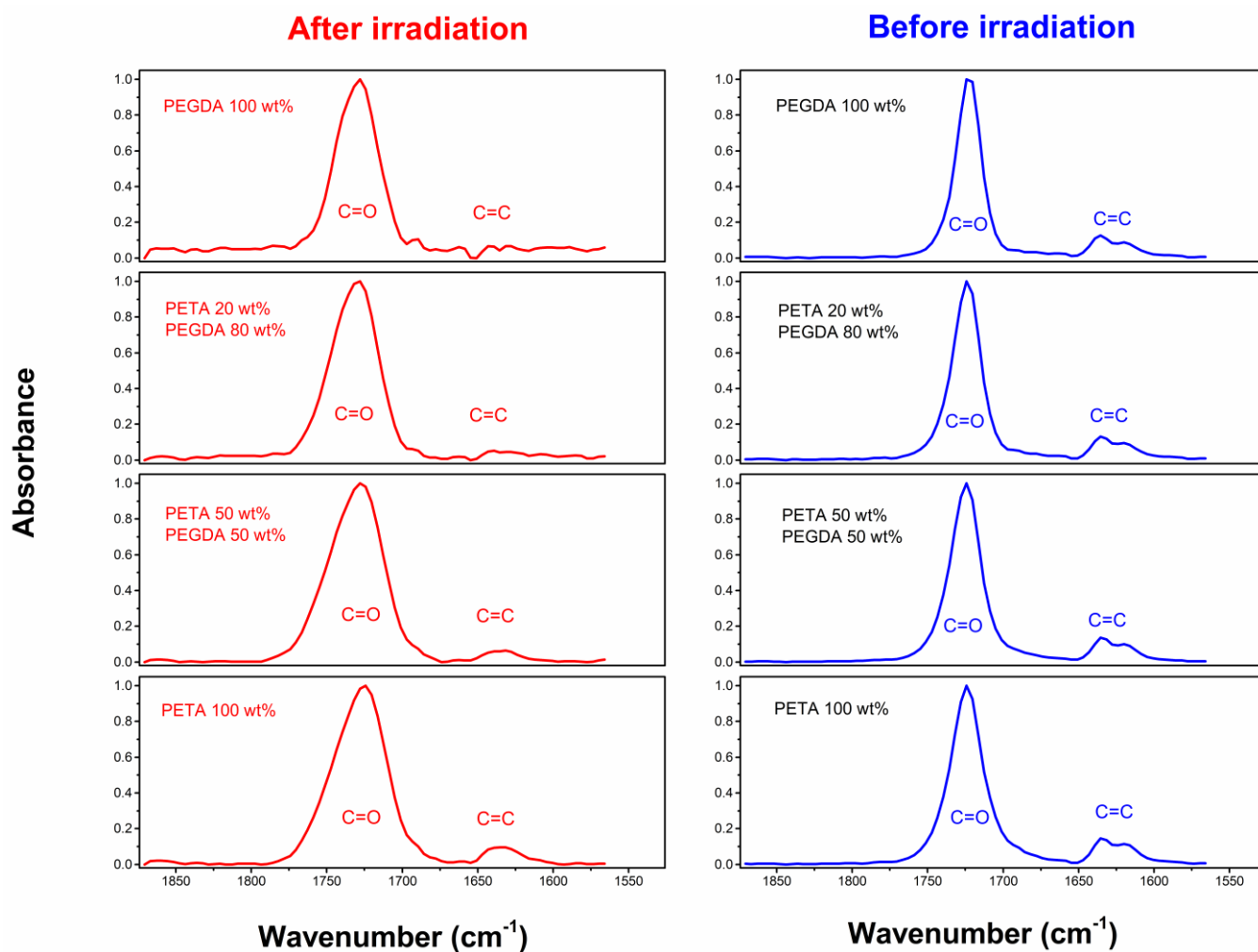
654
$$DC = \left[1 - \frac{A_{C=C}/A_{C=O}}{A'_{C=C}/A'_{C=O}} \right] \times 100 \quad (4)$$

655

656 with $A_{C=C}$, $A_{C=O}$, $A'_{C=C}$ and $A'_{C=O}$ the integrated area of absorption bands related to the C=C and C=O
657 moieties in the polymerized and the nonpolymerized resin, respectively.

658

659



660

661 **Figure S11** : FTIR spectra of resins with different weight percentages of PETA and PEGDA (blue
662 lines) and the corresponding two-photon polymerized squares (red lines, laser power 13.5 mW was used
663 for all squares).

664

665 References:

666 [1] L.J. Jiang, Y.S. Zhou, W. Xiong, et al. Two-photon polymerization: investigation of chemical and
667 mechanical properties of resins using Raman microspectroscopy. *Opt. Lett.* **2014**, 39 (10), 3034–3037

668

669